

Supplemental Material – Mechanical Properties of Soot Particles: The Impact of Crosslinked Polycyclic Aromatic Hydrocarbons

Laura Pascazio¹, Jacob W. Martin^{1,2}, Maria L. Botero³, Mariano Sirignano⁴, Andrea D'Anna⁴,
Markus Kraft^{1,2,5,*}

¹Department of Chemical Engineering and Biotechnology, University of Cambridge,
West Site, Philippa Fawcett Drive, Cambridge CB3 0AS, UK

²Cambridge Centre for Advanced Research and Education in Singapore (CARES)
CREATE Tower, 1 Create Way, Singapore, 138602

³Department of Mechanical Engineering, National University of Singapore
9 Engineering Drive, Singapore, 117576

⁴Dipartimento di Ingegneria Chimica, dei Materiali e della Produzione Industriale, Università degli Studi
di Napoli Federico II
Piazzale V. Tecchio 80, Napoli, 80125, Italy

⁵School of Chemical and Biomedical Engineering, Nanyang Technological University
62 Nanyang Drive, Singapore, 637459

*Corresponding Author: Markus Kraft e-mail: mk306@cam.ac.uk

S1. Force field benchmark

The AIREBO potential has been previously benchmarked to reproduce structural and energetic properties of both gaseous and liquid hydrocarbons as well as diamond and graphite properties (Stuart et al., 2000). The AIREBO potential has also been extensively used to study the mechanical properties of carbon materials (Stuart et al., 2000; Zhao et al., 2009; O'Connor et al., 2015; Rego and Meunier, 2019). Its modified version, AIREBO-M, where the Lennard-Jones potential has been replaced with a Morse potential, has been further optimised to improve intermolecular steric repulsions, while preserving the ambient thermodynamics of the original potential. The potential was fit to experimental measurements of the layer spacing of graphite up to 14 GPa and first principles calculations of steric interactions between small alkanes (O'Connor et al., 2015). Although the AIREBO and AIREBO-M force fields have been benchmarked in literature, we did our own benchmarking to be sure that the force field can accurately reproduce the elastic properties of carbonaceous materials. The force field has been benchmarked in two ways.

Firstly, we calculated the bond dissociation energies using the AIREBO-M force field and using the dispersion corrected hybrid density functional M06-2X-D3/cc-pVTZ. Bond energies can be compared to the bond enthalpy benchmark values (NIST thermodynamic database) as the thermal correction is minimal at <1 kcal/mol. The biphenyl C–C bond energy has a benchmark value of -117.6 kcal/mol (Tranter et al., 2010); DFT calculations provided a value of -119.4 kcal/mol and AIREBO-M force field provided a value of -124.1 kcal/mol, showing in both cases a slight overestimation of the bond energy ($+1.5\%$ and $+5.5\%$ respectively). The binaphthalene C–C bond energy using AIREBO-M has a value of -125.9 kcal/mol, again showing a slight overestimation of the bond energy that has been found to be -120 kcal/mol from DFT calculations.

Secondly, and more importantly for the scope of this work, we checked the bond breaking process. We calculated the yield point and Young's modulus of graphene and diamond as a benchmark using the same methodology reported in the main text (molecular dynamics simulations of uniaxial tensile deformation section). The results agree with previous modelling studies and experimental values (Table S1), indicating that AIREBO-M provides the correct elastic re-

sponse and that the Morse function used in this version of AIREBO ensures the correct asymmetric bond breaking potential surface. The calculated Young’s modulus and yield stress values are always within 5% of the benchmark values as reported in Table S1. It is important to note that the values reported for diamond in Table 1 and 2 in the main text are an average between the ones computed for the $\langle 100 \rangle$ and $\langle 111 \rangle$ directions and the HOPG values in Table 1 and 2 are reported for the direction perpendicular to the aromatic plane.

Table S1: *Young’s modulus, tensile yield stress and strain at which the yield stress occurs for diamond and graphite. The results are compared with previous calculations and experiments.*

Structure	Direction	Yield Strain	Yield Stress (GPa)	Young’s modulus (GPa)	Method	Ref.
Diamond	$\langle 111 \rangle$	0.131	92.6	1151	MD	(this work)
		0.13 (+0.8%)	90.8 (+2%)	-	DFT	Chen et al. (2007)
		-	-	1137 (+1.2%)	exp.	Richter et al. (2000)
Diamond	$\langle 100 \rangle$	0.155	83.4	897	MD	(this work)
		-	-	921 (-2.6%)	exp.	Richter et al. (2000)
Graphene	armchair	0.14	91.1	1051	MD	(this work)
		0.13 (+7.7%)	90 (+1.2%)	1010 (+4.1%)	MD	Zhao et al. (2009)
Graphene	zigzag	0.21	108.8	1012	MD	(this work)
		0.20 (+5.0%)	107 (+1.7%)	1010 (+0.2%)	MD	Zhao et al. (2009)
Graphene	in-plane	-	-	1000	exp.	Lee et al. (2008)

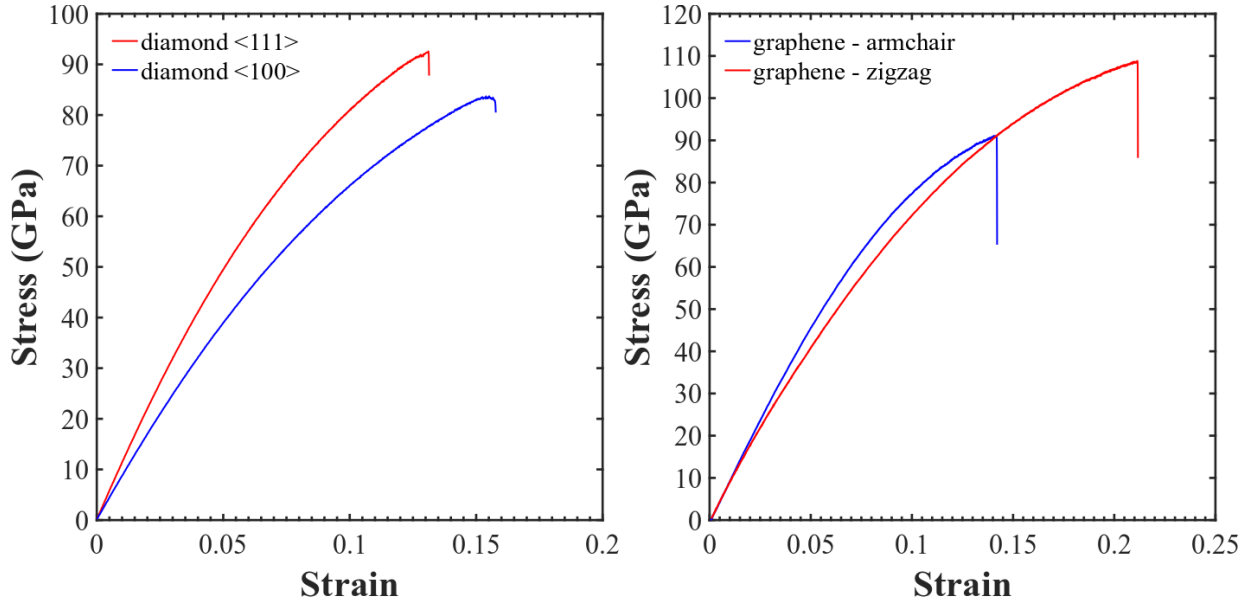


Figure S1: Stress-strain uniaxial tensile curves for diamond in the $\langle 111 \rangle$ and $\langle 100 \rangle$ directions (left) and for graphene in the armchair and zigzag directions (right).

S2. Effect of the strain rate

In order to investigate the effect of the strain rate on the tensile deformation, four different strain rates, i.e., $1 \cdot 10^{10} \text{ s}^{-1}$, $5 \cdot 10^9 \text{ s}^{-1}$, $1 \cdot 10^9 \text{ s}^{-1}$ and $5 \cdot 10^8 \text{ s}^{-1}$ were considered. Figure S2 shows the stress-strain curves at different strain rates for the coronene system with $CL = 3.05$. We find that as the strain rate increases from $5 \cdot 10^8 \text{ s}^{-1}$ to $1 \cdot 10^{10} \text{ s}^{-1}$, the peak strength increases from 4.1 GPa to 5 GPa, while the initial slope of the stress-strain curve is insensitive to the strain rate. The strain at the peak also increases with increasing strain rate. Because of the small changes in the stress-strain curves upon decreasing the strain rate from $1 \cdot 10^9 \text{ s}^{-1}$ (green line) to $5 \cdot 10^8 \text{ s}^{-1}$ (blue line), we assume that the results will not considerably change when decreasing the strain rate below $5 \cdot 10^8 \text{ s}^{-1}$ and a strain rate of $5 \cdot 10^8 \text{ s}^{-1}$ was used for all the simulations.

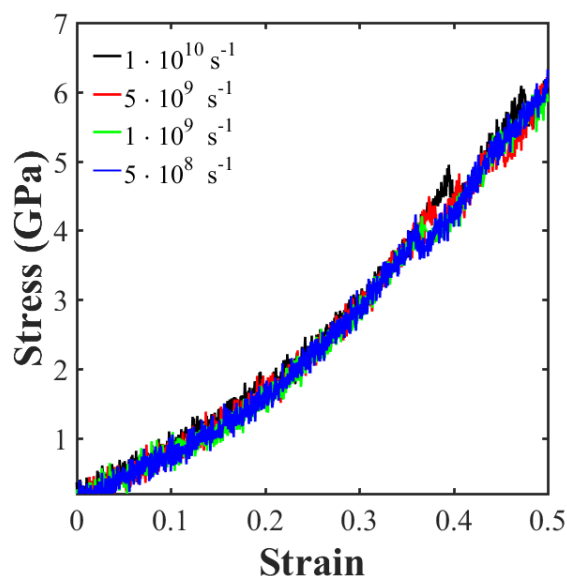


Figure S2: *Stress-strain curves of tensile deformation at different strain rates for coronene system with $CL = 3.05$.*

S3. Effect of particle density

The density of the systems investigated in the main text is 1.5 g/cm^3 . Soot density can reach values around 1.8 g/cm^3 , so higher density systems have been also tested for comparison. The CL increases more quickly in the crosslinking procedure for the systems with a higher density (Figure S3a and Figure S3b). Systems with the same CL but different densities provided the same yield stress and Young's modulus (slope of the linear part of the stress-strain curve before the yield stress point) values but they have different stress-strain curve shapes (Figure S3c and Figure S3d). The linear behaviour of the stress-strain curve of the high density systems indicates that all the new bonds are stretched at the same time at the start of the tensile test simulation.

When the density is lower the curve is J-shaped. The primary reason for these different elastic behaviours may be that the chains form random coils between the crosslink points within the 3D network when the density is lower. This depends on the larger distances between monomers that meet fewer reactive sites at the start of the simulation and form more 'folded' networks. Moreover, the high density does not permit the molecules to arrange in stacks during the equilibration time so that they are more randomly distributed in the volume and form links in all directions. By changing the density we created different network designs but the yield stress and

Young's modulus values were not affected, indicating that they depend exclusively on the CL of the structure.

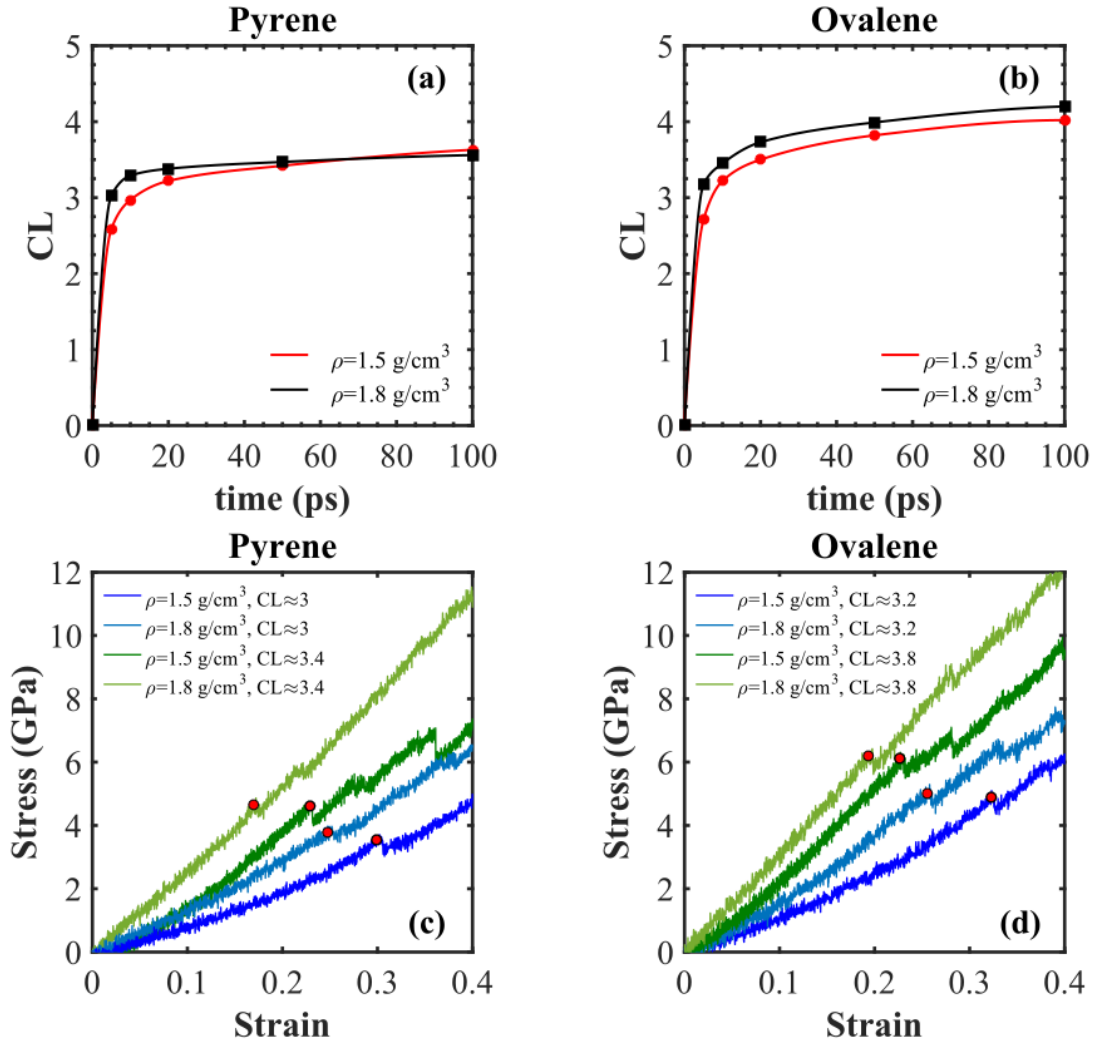


Figure S3: (a-b) Degree of crosslinking (CL) as a function of MD time and (c-d) Stress-strain curves of tensile deformation for low (1.5 g/cm^3) and high (1.8 g/cm^3) density systems at varying degrees of crosslinking (CL). Red circles represent the yield point in each system.

S4. Low CL systems

In Figure 3 (main text) the degree of crosslinking quickly increases, giving rise to structures with high degrees of crosslinking in the first picoseconds of the simulations due to the high number of reactive sites available in the crosslinking simulation. Here, fewer reactive sites were created in the simulation boxes by directly removing 1/4 (instead of 1/2 as in the main text) of the hydrogen atoms. The results are reported for the coronene system.

Figure S4 shows the CL versus time in both cases. As expected, systems with a lower CL were obtained starting from a lower number of reactive sites.

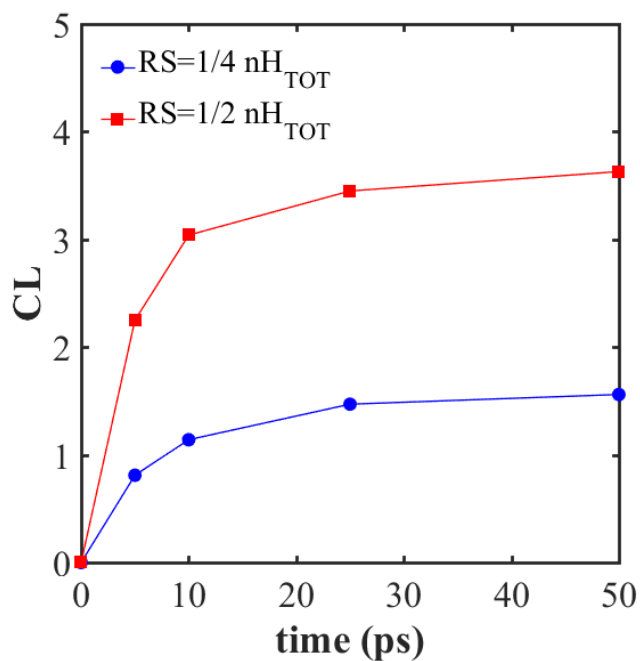


Figure S4: Degree of crosslinking (CL) as a function of MD time for coronene system starting from a different number of reactive sites (RS): the reactive sites are created by directly removing 1/4 of the starting hydrogen atoms (blue line) and 1/2 of hydrogen atoms (red line).

S5. Structural analysis

The aim of this study is to provide a link between the degree of crosslinking in the structure and mechanical properties. During the reactive MD simulations other reactions such as ring condensation, dehydrogenation and/or recombination of C–H bonds could occur. To be sure that only aliphatic crosslinking are forming in our system, the structures have been extensively checked at the end of the crosslinking MD simulation step before adding H atoms. Table S2 shows the percentage of broken bonds (C–C bond breakage and C–H bond breakage), the percentage of new bonds (crosslinks or other bonds) and the reaction occurrence in each system.

The proportion of bonds that break during the crosslinking procedure are always less than 0.5% and most of them are C–H bonds. A temperature of 1000 K ensures that a very small amount of the C–C bonds are broken. When a C–H breaks, a new reactive site is formed that can react and form other crosslinks in the structure and the H atoms can be involved in H migration or H abstractions reactions or remain in the system as a free radical. When a C–C bond breaks, ring opening reactions with a subsequent formation of aliphatic chains and/or new reactive sites as well as structural rearrangement can occur in the samples.

The main reaction detected in all the systems is the formation of crosslinks (>92% in all the considered systems). The second most common reaction is H abstraction by another reactive site that leads to the formation of a new reactive site (2-5%). The other reactions can be considered negligible. Ring condensations owing to H abstraction from a carbon atom next to a reactive site were not observed.

Table S2: (a) Percentage of conserved and broken bonds in relation to the number of bonds in the starting configuration and percentage of conserved and new bonds in relation to total number of bonds in each system. (b) Percentage of occurrence of each reaction type in relation to the total number of reaction events.

PAH	$C_{16}H_{10}$				$C_{24}H_{12}$					$C_{32}H_{14}$			
CL	0.00	2.60	2.95	3.40	0.00	2.25	3.05	3.65	3.75	0.00	2.70	3.20	3.80
(a) Bonds (%)													
Conserved bonds**	100	99.73	99.69	99.53	100	99.82	99.76	99.60	99.47	100	99.76	99.71	99.68
Broken bonds* C–C	0.00	0.04	0.04	0.04	0.00	0.04	0.04	0.06	0.07	0.00	0.09	0.09	0.09
C–H	0.00	0.22	0.27	0.43	0.00	0.14	0.20	0.34	0.46	0.00	0.15	0.20	0.23
Conserved bonds**	100	94.27	93.59	92.63	100	96.56	95.62	94.76	94.46	100	96.98	96.59	95.95
New bonds* crosslinks	0.00	5.52	6.14	7.01	0.00	3.30	4.19	4.94	5.14	0.00	4.40	4.44	4.81
other bonds	0.00	0.21	0.27	0.36	0.00	0.14	0.19	0.30	0.40	0.00	0.20	0.22	0.25
(b) Reactions (%)													
1) Formation of crosslinks	0.00	96.31	95.73	95.12	0.00	95.95	95.76	94.28	92.70	0.00	93.13	93.44	93.84
2) H abstraction	0.00	2.31	2.46	3.11	0.00	2.65	2.91	3.51	4.45	0.00	4.52	4.64	4.42
3) H migration	0.00	0.28	0.49	0.42	0.00	0.31	0.36	0.40	0.47	0.00	0.18	0.16	0.00
4) Formation of H*	0.00	0.00	0.00	0.00	0.00	0.00	0.00	0.00	0.00	0.00	0.36	0.00	0.00
5) Structural defect and/or ring opening	0.00	1.11	1.31	1.34	0.00	1.09	0.97	1.81	2.37	0.00	1.81	1.76	1.74
6) Cyclodehydrogenation	0.00	0.00	0.00	0.00	0.00	0.00	0.00	0.00	0.00	0.00	0.00	0.00	0.00

* in relation to the number of bonds in the starting configuration

** in relation to the number of bonds in the system

References

- Chen, S., Gong, X. G. and Wei, S. H. (2007), ‘Superhard Pseudocubic BC₂N Superlattices’, *Physical Review Letters* **98**(1), 015502.
- Lee, C., Wei, X., Kysar, J. and Hone, J. (2008), ‘Measurement of the elastic properties and intrinsic strength of monolayer graphene’, *Science* **321**, 385–388.
- O’Connor, T. C., Andzelm, J. and Robbins, M. O. (2015), ‘AIREBO-M: A reactive model for hydrocarbons at extreme pressures’, *The Journal of Chemical Physics* **142**(2), 024903.
- Rego, K. and Meunier, V. (2019), ‘Carbon nanotube knots’, *AIP Advances* **9**, 025030.
- Richter, A., Riesa, R., Smith, R., Henkel, M. and Wolf, B. (2000), ‘Nanoindentation of diamond, graphite and fullerene films’, *Diamond and Related Materials* **9**, 170–184.
- Stuart, S. J., Tutein, A. B. and Harrison, J. A. (2000), ‘A reactive potential for hydrocarbons with intermolecular interactions’, *The Journal of Chemical Physics* **112**(14), 6472–6486.
- Tranter, R. S. and Klippenstein, S. J., Harding, L. B., Giri, B. R., Yang, X. and Kiefer, J. H. (2010), ‘Experimental and theoretical investigation of the self-reaction of phenyl radicals’, *The Journal of Physical Chemistry A* **114**(32), 8240–8261.
- Zhao, H., Min, K. and Aluru, N. R. (2009), ‘Size and Chirality Dependent Elastic Properties of Graphene Nanoribbons under Uniaxial Tension’, *Nano Letters* **9**(8), 3012–3015.